

Uncertainty-Aware Testing-Time Optimization for 3D Human Pose Estimation

Ti Wang¹, Mengyuan Liu^{1,*}, Hong Liu¹, Bin Ren², Yingxuan You¹, Wenhao Li¹, Nicu Sebe², Xia Li³

¹National Key Laboratory of General Artificial Intelligence, Peking University, Shenzhen Graduate School

²University of Trento ³Department of Computer Science, ETH Zürich

{tiwang, youyx}@stu.pku.edu.cn nkliuyifang@gmail.com {wenhao, hongliu}@pku.edu.cn

xia.li@inf.ethz.ch niculae.sebe@unitn.it

Abstract

Although data-driven methods have achieved success in 3D human pose estimation, they often suffer from domain gaps and exhibit limited generalization. In contrast, optimization-based methods excel in fine-tuning for specific cases but are generally inferior to data-driven methods in overall performance. We observe that previous optimization-based methods commonly rely on projection constraint, which only ensures alignment in 2D space, potentially leading to the overfitting problem. To address this, we propose an Uncertainty-Aware testing-time Optimization (UAO) framework, which keeps the prior information of pre-trained model and alleviates the overfitting problem using the uncertainty of joints. Specifically, during the training phase, we design an effective 2D-to-3D network for estimating the corresponding 3D pose while quantifying the uncertainty of each 3D joint. For optimization during testing, the proposed optimization framework freezes the pre-trained model and optimizes only a latent state. Projection loss is then employed to ensure the generated poses are well aligned in 2D space for high-quality optimization. Furthermore, we utilize the uncertainty of each joint to determine how much each joint is allowed for optimization. The effectiveness and superiority of the proposed framework are validated through extensive experiments on two challenging datasets: Human3.6M and MPI-INF-3DHP. Notably, our approach outperforms the previous best result by a large margin of 4.5% on Human3.6M. Our source code will be open-sourced.

1. Introduction

Monocular 3D human pose estimation aims to estimate 3D body joints from a single image. This task plays an important role in various applications, such as computer animation [36], human-computer interaction [29], and action recognition [19], but, due to the depth ambiguity, it is still a challenging

*Corresponding Author.

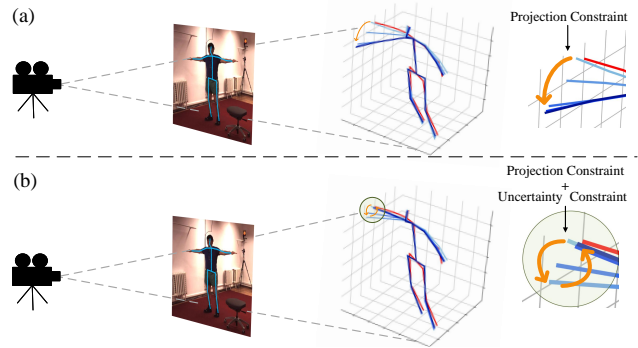


Figure 1. Schematic diagram of the iterative optimization process for human pose estimation. The red pose represents the ground truth, and the blue pose represents our predicted result. The intensity of color corresponds to the number of iterations, with darker colors indicating more iterations. In (a), poses generated by projection constraints are presented. We observe that the projection constraint alone can sometimes mislead the optimization direction, resulting in the optimized 3D pose far from the ground truth (the red pose). In (b), the introduce of uncertainty constraint effectively alleviates this problem.

task that has drawn extensive attention in recent years.

With the development of deep learning, data-driven methods [2, 18, 21, 42, 47] outperform traditional methods and have dominated the field of 3D human pose estimation. During the training process, these methods implicitly acquire knowledge of camera intrinsic parameters and 3D human pose distributions within specific domains. However, these data-driven methods struggle with cross-domain generalization and in-the-wild scenarios [5, 7].

Historically, traditional solutions usually formulate the 3D human pose estimation task as a pure optimization-based problem [24, 26, 33]. Recently, some human mesh recovery methods [8, 12, 14, 15] also adopted optimization strategies to optimize network parameters based on certain constraints. Optimization-based methods offer two significant benefits. First, they prevent the model from generating unrealistic

or out-of-distribution poses, which ultimately boosts the model’s robustness. Second, optimization-based approaches offer the flexibility of adaptive adjustments tailored for specific samples, thereby enhancing the model’s generalization capabilities. While optimization-based methods can alleviate domain gaps by estimating 3D poses on a case-by-case basis, their current performance is inferior to data-driven methods. We observe that the previous optimization-based methods [12, 15, 41] typically rely only on the projection constraint. However, due to the inherent depth ambiguity [18], several potential 3D poses could be projected to the same 2D pose. While alignment in 2D space is assured, this imperfect constraint may lead to overfitting during optimization. Additionally, previous optimization-based methods typically employ pre-trained networks to obtain a good initialization, subsequently optimizing the network parameters. Nevertheless, this approach involves a vast number of parameters to be optimized, which may disrupt the prior information embedded in the pre-trained network.

To solve the above problems, we propose an Uncertainty-Aware testing-time Optimization (UAO) framework for 3D human pose estimation. This optimization framework retains the prior knowledge embedded in the pre-trained model and alleviates the overfitting problem using uncertainty of joints. Specifically, we design an effective network for 2D-to-3D pose lifting, and employ a separate decoder to obtain the uncertainty associated with each joint. In this way, our network can simultaneously generate the 3D results and the uncertainty of each joint based on input 2D pose during the training phase. For the testing-time optimization, our target is to make the optimized poses more reliable. Different from previous optimization-based methods that optimize network parameters, the designed optimization strategy freezes the network parameters and optimizes a latent state. This design has two benefits: a) fixing the network parameters can keep the learned pose prior during the optimization process; b) setting the optimization target as a hidden state instead of the network parameter only requires the storage of a small number of parameters, making it more suitable for online inference scenarios. Furthermore, our optimization process incorporates a set of well-designed constraints to guide the optimization direction. For 2D pose alignment, we adopt the camera intrinsic parameters to project the generated 3D pose to 2D space and then minimize the projection loss. Since we do not know the depth information or ground truth, it is hard to get the 3D alignment. We discover that projection constraints may result in overfitting problems, causing the optimized 3D pose to deviate more from the ground truth. To alleviate this, we propose uncertainty constraint that allows 3D joint with higher uncertainty to have a larger degree of optimization, while keeping joint with smaller uncertainty in its original position. As shown in Figure 1, relying solely on

projection constraint may inadvertently lead to an incorrect optimization direction, producing worse results. This issue is effectively mitigated when we further introduce uncertainty constraints. With such a unique design, the optimization process is prevented from generating physically implausible poses, leading to more realistic and accurate results.

Our contributions can be summarized as follows:

- We propose a novel Uncertainty-Aware testing-time Optimization (UAO) framework for 3D human pose estimation, which freezes the pre-trained model to maintain the pose prior and utilize the uncertainty of joints to alleviate the overfitting problem.
- We design an effective 2D-to-3D lifting network, which can both 3D output while estimating the uncertainty of each joint.
- For test time optimization, projection constraint is used to ensure that the generated results are aligned in the 2D pose. Furthermore, we design the uncertainty constraint to determine the degree to which each joint can be optimized, which alleviates the overfitting problem.
- Extensive experiments demonstrate the effectiveness of the proposed UAO framework, and the potential applicability for real-world scenarios.

2. Related Work

Existing single-view 3D human pose estimation methods fall into two primary categories: a) direct estimation [20, 22, 28]: infer a 3D human pose from 2D images without the need for intermediate 2D pose representation, b) 2D-to-3D lifting [2, 23, 39, 43]: infer a 3D human pose from an intermediately estimated 2D pose. Benefiting from the success of 2D pose detectors [3, 27], the 2D-to-3D lifting approaches generally outperform the direct estimation approaches in both efficiency and effectiveness, becoming the mainstream approach. In this work, our approach follows the 2D-to-3D lifting pipeline, which can be further categorized into data-driven and optimization-based methods.

Data-driven methods. Data-driven approaches involve training a deep neural network to directly regress 3D human poses from provided 2D poses. Early attempts simply use fully-connected networks (FCNs) to lift the 2D keypoint to 3D space [21]. Since the human skeleton can be naturally represented as a graph, various graph convolutional networks (GCNs) based methods [2, 9, 35, 44, 47] have been proposed. Recently, transformer-based methods [17, 18, 42, 46] have been widely applied to 3D human pose estimation, achieving new breakthroughs. Although these methods can effectively learn pose patterns from datasets, they often exhibit poor generalization ability when faced with unseen data.

Optimization-based methods. During the early stages, researchers employed pure optimization-based methods [24, 26, 33] for 3D human pose estimation. In the era of deep learning, there are also some methods that inte-

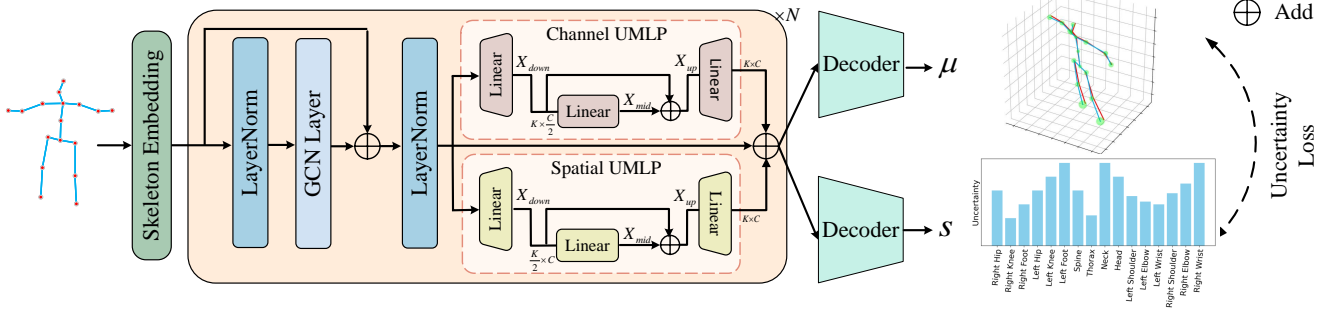


Figure 2. Structure of the GUMLP model. Initially, the 2D input is first transformed into high-dimensional features through skeleton embedding. Subsequently, the GCN layer captures the graph information from the high-dimensional features. Then the Channel UMLP and Spatial UMLP are utilized to capture the multi-level and multi-scale information of the skeleton. Finally, two decoders are employed to predict the mean pose μ and the uncertainty value \mathbf{s} of the corresponding 3D pose distribution. The model is trained using uncertainty loss, which is calculated based on μ and \mathbf{s} .

grate optimization strategies. We categorize the existing optimization-based methods into two classes. 1) The first class incorporates a regression-based network with optimization strategies, training the entire structure end-to-end, such as SPIN [15] and PyMAF [40]. 2) The second class follows a post-optimization manner, which is more similar to us, using a pre-trained network to obtain a good initialization, including ISO [41], BOA [8], and EFT [12]. However, all these previous post-optimization methods typically optimize the network parameters based on specific constraints, which may disrupt the deep prior knowledge obtained from datasets. As a comparison, we set the optimization variable as the latent state, and keep the model parameters frozen during the iterative optimization process. Besides, pose-related constraints are imperative to ensure the appropriate optimization direction. Previous optimization-based methods simply rely on the projection constraint [12, 15, 41]. But due to the depth ambiguity, this imperfect constraint may lead to the wrong optimization direction when over-optimized. To alleviate this problem, we further utilize the uncertainty constraint to ensure that the generated pose lies within the manifold of 3D poses.

3. Uncertainty Estimation

For 2D-to-3D lifting, data-driven methods regress the 3D human pose $\mathbf{J}^{3D} \in \mathbb{R}^{K \times 3}$ from given 2D pose $\mathbf{J}^{2D} \in \mathbb{R}^{K \times 2}$, where K is the number of skeleton joints. They typically train the model to learn the transformational relationship between 2D pose \mathbf{J}^{2D} and ground truth 3D pose \mathbf{J}^{3D} by minimizing:

$$L_{2D} = \|\hat{\mathbf{J}}^{3D} - f(\mathbf{J}^{2D})\|_2, \quad (1)$$

where f denotes the 2D-to-3D lifting network for 3D human pose estimation. Although this loss function allows the pre-trained model to implicitly encode inherent patterns for

2D-to-3D lifting and acquire distribution features from the training set, it can not be aware of the uncertainty of each estimated joint. In order to enable the model to predict the uncertainty of each predicted joint, we reformulate the 2D-to-3D network as a Bayesian Neural Network (BNN) [13], which estimates a Gaussian distribution of the target rather than only predicting the absolute coordinates of points.

Specifically, for the k -th joint of the i -th person, we let the network predict the expected position $\mu_{i,k} \in \mathbb{R}^3$ and a simplified scalar covariance $\sigma_{i,k}$ from the input 2D pose \mathbf{J}^{2D} . By maximizing the likelihood of the training pairs, the loss function to train the BNN over the i -th person can be formulated as:

$$\begin{aligned} L_i^{train} &= \frac{1}{2K} \sum_{k=1}^K \left(\frac{\|\mathbf{J}_{i,k}^{3D} - \mu_{i,k}\|^2}{\sigma_{i,k}^2} + \ln \sigma_{i,k}^2 \right) \\ &= \frac{1}{2K} \sum_k (\|\mathbf{J}_{i,k}^{3D} - \mu_{i,k}\|^2 \exp(-\mathbf{s}_{i,k}) + \mathbf{s}_{i,k}), \end{aligned} \quad (2)$$

where we substitute $\ln \sigma_{i,k}^2$ with $\mathbf{s}_{i,k}$ for numerical stability during the training process.

To achieve this, we propose GUMLP, primarily consisting of two parts: a GCN layer and a parallel U-shaped multi-layer perception (UMLP) module, as shown in Figure 2. In contrast to the conventional data-driven model [21, 47], which typically employs only one decoder to make direct predictions, we utilize two distinct decoders to predict μ and \mathbf{s} , respectively. The GCN layer focuses on local joint relations and introduces the topological priors of the human skeleton. For the second component, the UMLP module has a bottleneck structure [2, 25] instead of the original MLP in the transformer [32]. The input of the UMLP module \mathbf{X} is first processed by a down-projection layer, followed by a middle layer that maintains the same dimension, and ultimately, is fed into an up-projection layer. The simplified

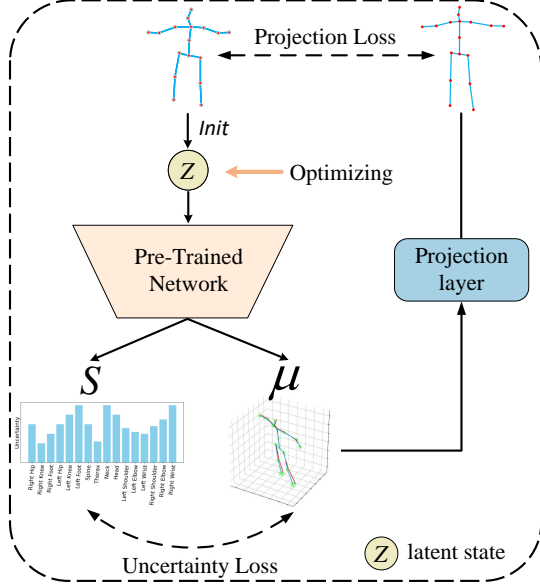


Figure 3. Structure of the UAO framework. During the testing-time optimization, the parameters of the pre-trained model (GUMLP) are frozen. The variable being optimized is the latent state \mathbf{z} , which is initialized with the original 2D pose input \mathbf{J}^{2D} . We use the pre-trained GUMLP to obtain the mean pose $\boldsymbol{\mu}$ and uncertainty value \mathbf{s} of the corresponding 3D pose distribution. The predicted mean pose is projected back to 2D space and compared with the input pose \mathbf{J}^{2D} to calculate the projection loss. The uncertainty loss is then calculated using $\boldsymbol{\mu}$ and \mathbf{s} . Under the constraints of projection and uncertainty, the latent state \mathbf{z} is optimized during the iterations.

formulation can be defined as:

$$\begin{aligned} \mathbf{X}_{down} &= \text{MLP}_{down}(\text{LN}(\mathbf{X})), \\ \mathbf{X}_{mid} &= \text{MLP}_{mid}(\mathbf{X}_{down}) + \mathbf{X}_{down}, \\ \mathbf{X}_{up} &= \text{MLP}_{up}(\mathbf{X}_{mid}) + \mathbf{X}, \end{aligned} \quad (3)$$

where $\text{MLP}(\cdot)$ consists of a linear layer and a GELU activation [10], LN denotes the Layer Normalization [1]. Here we adopt the parallel UMLP modules along both channel and spatial dimensions to capture multi-scale and multi-level features.

4. Testing-Time Optimization

4.1. Optimization Strategy

The proposed Uncertainty-Aware testing-time Optimization (UAO) framework is illustrated in Figure 3. It is essential to highlight that we only optimize the latent state $\mathbf{z} \in \mathbb{R}^{K \times 2}$ initialized by 2D input \mathbf{J}^{2D} . The parameters of the pre-trained model are fixed throughout the inference, which ensures the learned implicit prior from the training dataset not disrupted. Besides, we incorporate constraints into the optimization

Algorithm 1 Optimization Strategy

Input: 2D pose \mathbf{J}_j^{2D} , pre-trained model f^* with fixed parameters, projection matrix \mathbf{P} , optimization steps T

Output: 3D pose $\hat{\mathbf{J}}_j^{3D}$

- 1: Initialization: $\mathbf{z}_j = \mathbf{J}_j^{2D}$, $iter = 0$
- 2: $\hat{\boldsymbol{\mu}}_j = f_{\boldsymbol{\mu}}^*(\mathbf{J}_j^{2D})$, $\hat{\mathbf{s}}_j = f_{\mathbf{s}}^*(\mathbf{J}_j^{2D})$
- 3: **while** $iter < T$ **do**
- 4: $\hat{\mathbf{J}}_j^{3D} = f_{\boldsymbol{\mu}}^*(\mathbf{z}_j)$
- 5: $L_P^{opt} = \|\hat{\mathbf{J}}_j^{3D} \cdot \mathbf{P} - \mathbf{J}_j^{2D}\|_2$
- 6: $L_U^{opt} = \|\hat{\boldsymbol{\mu}}_j - \hat{\mathbf{J}}_j^{3D}\|^2 / (2 \cdot \exp(\hat{\mathbf{s}}_j))$
- 7: $L_{total}^{opt} = \lambda_P \cdot L_P^{opt} + \lambda_U \cdot L_U^{opt}$
- 8: $\mathbf{z}_j \leftarrow \text{Adam}(\mathbf{z}_j, \nabla L_{total}^{opt})$
- 9: $iter = iter + 1$
- 10: **end while**
- 11: $\hat{\mathbf{J}}_j^{3D} = f_{\boldsymbol{\mu}}^*(\mathbf{z}_j)$
- 12: **return** $\hat{\mathbf{J}}_j^{3D}$

process. Specifically, projection constraint is applied to guarantee alignment of the optimized 3D pose in 2D space, and uncertainty constraint is introduced to determine the degree to which each joint can be optimized. After several iterations, the latent state \mathbf{z} is refined progressively towards its optimal state. Ultimately, by feeding the optimized \mathbf{z}^* into the pre-trained network, we obtain a high-quality 3D pose. The pseudo-code of the testing-time optimization is summarized in Algorithm 1.

4.2. Projection Constraint

Projection constraint is commonly used in optimization-based methods, such as SPIN [15] and EFT [12]. For a given 3D pose \mathbf{J}^{3D} , its 2D projection \mathbf{J}^{2D} should conform to the principles of perspective projection [33], which can be expressed as follow:

$$\mathbf{J}^{3D} \cdot \mathbf{P} = \mathbf{J}^{2D}, \quad (4)$$

where the projection matrix $\mathbf{P} \in \mathbb{R}^{3 \times 2}$ contains the intrinsic parameters of the camera. In real scenarios, the intrinsic parameters of the camera can be obtained from camera specifications or can be inferred solely from the input images [34]. During the testing-time optimization, the 2D projection $\hat{\mathbf{J}}^{2D} = \hat{\mathbf{J}}^{3D} \cdot \mathbf{P}$ of the predicted 3D pose $\hat{\mathbf{J}}^{3D}$ is expected to closely align with the given 2D pose \mathbf{J}^{2D} . A large error between them indicates that the estimated 3D pose $\hat{\mathbf{J}}^{3D}$ may be problematic and needs to be corrected. The formulation of projection constraint can be expressed as:

$$L_P^{opt} = \|\hat{\mathbf{J}}^{2D} - \mathbf{J}^{2D}\|_2. \quad (5)$$

The purpose of the projection constraint is to enforce the relationship between the estimated 3D pose $\hat{\mathbf{J}}^{3D}$ and its

Table 1. Quantitative comparison with the state-of-the-art methods on Human3.6M under Protocol 1. Top-table: 2D pose detected by cascaded pyramid network (CPN) [3] is used as input. Bottom-table: Ground truth 2D pose is used as input. The top two best results for each action are highlighted in bold and underlined, respectively. § denotes the methods that use the same refinement module as [2, 47].

Method	Dire.	Disc.	Eat	Greet	Phone	Photo	Pose	Purch.	Sit	SitD.	Smoke	Wait	WalkD.	Walk	WalkT.	Avg
SimpleBaseline (ICCV'2017) [21]	51.8	56.2	58.1	59.0	69.5	78.4	55.2	58.1	74.0	94.6	62.3	59.1	65.1	49.5	52.4	62.9
VideoPose3D (CVPR'2019) [23]	47.1	50.6	49.0	51.8	53.6	61.4	49.4	47.4	59.3	67.4	52.4	49.5	55.3	39.5	42.7	51.8
LCN (ICCV'2019) [4]	46.8	52.3	<u>44.7</u>	50.4	52.9	68.9	49.6	46.4	60.2	78.9	51.2	50.0	54.8	40.4	43.3	52.7
STGCN (ICCV'2019) [2] §	46.5	48.8	47.6	50.9	52.9	61.3	48.3	45.8	59.2	64.4	51.2	48.4	53.5	39.2	41.2	50.6
SRNet (ECCV'2020) [37]	44.5	48.2	47.1	47.8	51.2	<u>56.8</u>	50.1	45.6	59.9	66.4	52.1	45.3	54.2	39.1	<u>40.3</u>	49.9
GraphSH (CVPR'2021) [35]	45.2	49.9	47.5	50.9	54.9	66.1	48.5	46.3	59.7	71.5	51.4	48.6	53.9	39.9	44.1	51.9
MGCN (ICCV'2021) [47] §	45.4	49.2	45.7	49.4	50.4	58.2	47.9	46.0	57.5	63.0	49.7	46.6	52.2	38.9	40.8	<u>49.4</u>
GraFormer (CVPR'2022) [45]	45.2	50.8	48.0	50.0	54.9	65.0	48.2	47.1	60.2	70.0	51.6	48.7	54.1	39.7	43.1	51.8
UGRN (AAAI'2023) [16]	47.9	50.0	47.1	51.3	51.2	59.5	48.7	46.9	<u>56.0</u>	<u>61.9</u>	51.1	48.9	54.3	40.0	42.9	50.5
MLP-JCG (TMM'2023) [30]	<u>43.8</u>	46.7	46.9	<u>48.9</u>	<u>50.3</u>	60.1	45.7	<u>43.9</u>	<u>56.0</u>	73.7	<u>48.9</u>	48.2	<u>50.9</u>	39.9	41.5	49.7
GUMLP (Ours)	44.3	49.8	<u>44.7</u>	49.3	51.4	58.1	47.3	45.6	58.2	63.7	51.0	47.6	53.4	<u>38.1</u>	40.4	49.5
GUMLP + UAO (Ours)	42.3	<u>47.7</u>	42.8	47.8	48.7	55.8	<u>45.8</u>	42.4	55.2	60.9	48.6	<u>45.9</u>	50.2	36.0	38.2	47.2
Method	Dire.	Disc.	Eat	Greet	Phone	Photo	Pose	Purch.	Sit	SitD.	Smoke	Wait	WalkD.	Walk	WalkT.	Avg
SimpleBaseline (ICCV'2017) [21]	37.7	44.4	40.3	42.1	48.2	54.9	44.4	42.1	54.6	58.0	45.1	46.4	47.6	36.4	40.4	45.5
STGCN (ICCV'2019) [2]	33.4	39.0	33.8	37.0	38.1	47.3	39.5	37.3	43.2	46.2	37.7	38.0	38.6	30.4	32.1	38.1
LCN (ICCV'2019) [4]	36.3	38.8	<u>29.7</u>	37.8	<u>34.6</u>	42.5	39.8	32.5	<u>36.2</u>	<u>39.5</u>	34.4	38.4	38.2	31.3	34.2	36.3
MGCN (ICCV'2021) [47]	-	-	-	-	-	-	-	-	-	-	-	-	-	-	-	37.4
GraFormer (CVPR'2022) [45]	32.0	38.0	30.4	34.4	34.7	43.3	35.2	31.4	38.0	46.2	34.2	35.7	36.1	<u>27.4</u>	30.6	35.2
MLP-JCG (TMM'2023) [30]	29.1	<u>36.0</u>	30.4	<u>33.8</u>	35.5	46.5	35.3	<u>31.2</u>	39.2	48.8	<u>33.9</u>	<u>35.2</u>	<u>35.8</u>	26.9	<u>29.4</u>	35.1
GUMLP (Ours)	30.2	36.2	30.3	32.9	33.6	<u>41.6</u>	<u>35.1</u>	31.8	38.7	42.6	34.8	36.8	37.2	28.7	30.0	<u>34.7</u>
GUMLP + UAO (Ours)	<u>29.5</u>	34.5	27.5	31.1	31.8	38.4	34.0	29.6	35.5	38.7	32.9	35.0	34.9	28.1	29.2	32.7

corresponding 2D projection $\hat{\mathbf{J}}^{2D}$ to follow the geometric principles of perspective projection, thereby improving the accuracy of the pose estimation.

4.3. Uncertainty Constraint

Although the projection constraint can ensure the alignment of the generated pose in 2D space, it often brings over-fitting problems. This is due to the fact that multiple 3D poses might correspond to the same 2D pose after projection, which is an inherent challenge in the 3D human pose estimation task. When we solely depend on the projection constraint for the optimization process, we observe two phenomena: 1) some joints that were well-estimated deviate away from the ground truth; 2) some poorly estimated joints are initially close to the ground truth but then move away from it. To alleviate this, we introduce uncertainty constraint, which allows the well-estimated joints to stay in their original positions and mainly optimize the joints with high uncertainties.

During the testing process, for the j -th 2D input, the pre-trained model allows us to acquire the initial 3D result $\hat{\boldsymbol{\mu}}_k$ and uncertainty $\hat{\boldsymbol{s}}_k$ associated with the k -th estimated 3D joint. We can explicitly express the uncertainty constraint as:

$$\mathcal{L}_{U,j}^{opt} = \frac{1}{2K} \sum_{k=1}^K \|\hat{\boldsymbol{\mu}}_{j,k} - f_{\boldsymbol{\mu}}^*(\mathbf{z})_{j,k}\|^2 \exp(-\hat{\boldsymbol{s}}_{j,k}), \quad (6)$$

where f^* denotes the pre-trained model, $f_{\boldsymbol{\mu}}$ denotes the predicted 3D result. This constraint enables joints with higher uncertainty less constrained by the results of the initial estimation, allowing more room for optimization. On the other

hand, the joint with lower uncertainty means that the network is confident about the result, so limit it from further drifting.

5. Experiments

5.1. Datasets and Evaluation Metrics

Here, we provide a more detailed description of the datasets and evaluation metrics.

Human3.6M is the most representative benchmark for 3D human pose estimation. It contains 3.6 million video frames captured from four synchronized cameras at 50Hz in an indoor environment. There are 11 professional actors performing 17 actions, such as greeting, phoning, and sitting. Following previous works [2, 23], we train our model on five subjects (S1, S5, S6, S7, S8) and test it on two subjects (S9 and S11). The performance is evaluated by two common metrics: MPJPE (Mean Per-Joint Position Error), termed Protocol 1, is the mean Euclidean distance between the predicted joints and the ground truth in millimeters. P-MPJPE, termed Protocol 2, is the MPJPE after rigid alignment with the ground truth in translation, rotation, and scale.

MPI-INF-3DHP is a more challenging 3D pose dataset that contains both indoor and complex outdoor scenes. There are 8 actors performing 8 actions from 14 camera views, which cover a greater diversity of poses. Its test set consists of three different scenes: studio with green screen (GS), studio without green screen (noGS), and outdoor scene (Outdoor). Following [23, 38, 47], we use Percentage of Correct Key-points (PCK) with a threshold of 150mm and the Area Under Curve (AUC) for a range of PCK thresholds for evaluation.

Table 2. Quantitative comparisons with state-of-the-art methods on the MPI-INF-3DHP dataset.

Method	GS \uparrow	noGS \uparrow	Outdoor \uparrow	All PCK \uparrow	All AUC \uparrow
SimpleBaseline [21]	49.8	42.5	31.2	42.5	17.0
GraphSH [35]	81.5	81.7	75.2	80.1	45.8
MGCN [47]	86.4	86.0	85.7	86.1	53.7
GraFormer [45]	80.1	77.9	74.1	79.0	43.8
UGRN [16]	86.2	84.7	81.9	84.1	53.7
GUMLP (Ours)	87.6	86.1	87.1	87.0	54.3
GUMLP + UAO (Ours)	89.2	87.7	87.9	88.2	54.5

5.2. Implementation Details

We implement our approach with PyTorch, training and testing it on one NVIDIA RTX 3090 GPU. Following [2, 47], we use 2D pose detected by CPN [3] for Human3.6M, and ground truth 2D pose for MPI-INF-3DHP. Horizontal flipping is used as data augmentation following [2, 37, 47]. During the training phase, we train a deep neural network for deep prior. The proposed GUMLP is designed by stacking GCN layers and UMLP modules for $N = 4$ times. Adam optimizer is adopted with an initial learning rate of 0.001 and a decay factor of 0.95 per epoch. For the testing time optimization, the hyperparameters for projection loss and uncertainty loss are chosen as $\lambda_P = 1$ and $\lambda_U = 0.005$, respectively.

5.3. Comparison with State-Of-the-Art Methods

Human3.6M. The comparison results with other state-of-the-art methods under Protocol 1 are shown in Table 1. Following [2, 35, 47], the 2D pose detected by CPN [3] is used as input for training and testing. It is worth mentioning that the previous state-of-the-art method, MGCN [47], incorporated a refinement module to enhance performance. However, even without this module, our baseline model GUMLP achieves a comparable accuracy, with only a marginal difference of 0.1mm. Furthermore, by integrating the Uncertainty-Aware testing-time Optimization (UAO) framework, which leverages both projection and uncertainty constraints, the performance of GUMLP is significantly improved (from 49.5mm to 47.2mm, a relative 4.6% improvement). Notably, GUMLP with UAO framework outperforms MGCN [47] by 4.5% (49.4mm vs. 47.2mm). For Protocol 2, we also obtain the best overall results (39.0mm, see supplemental material). These results validate the effectiveness of the designed 2D-to-3D lifting network (GUMLP) and the UAO framework. To further explore the lower bounds of our approach, we compare our approach with previous state-of-the-art methods with ground truth 2D pose as input. As shown in Table 1 (bottom), we achieve state-of-the-art performance, outperforming all other methods. Furthermore, we observe that the performance of GUMLP can still be boosted with the UAO framework, even when the latent state z is initialized

Table 3. Ablation study on proposed constraints in 5 iterations step using BOA framework.

Pre-trained Model	Projection Constraint	Uncertainty Constraint	MPJPE \downarrow
\checkmark			49.5
\checkmark	\checkmark		48.2
\checkmark	\checkmark	\checkmark	47.2

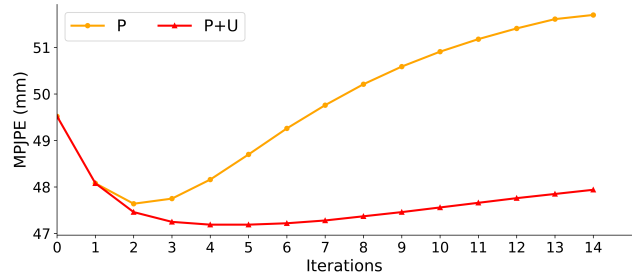


Figure 4. Performance with different iterations on Human3.6M test set. Here we adopt the pre-trained GUMLP as baseline and use the 2D pose detected by CPN [3] to initialize the latent state z . P and U represent projection constraint and uncertainty constraint, respectively.

with the ground truth 2D pose. This is due to the insufficient capacity of the pre-trained GUMLP, and the use of projection constraint and uncertainty constraint during the optimization process can effectively enhance the quality of generated 3D poses.

MPI-INF-3DHP. To evaluate the generalization ability of the proposed UAO framework, we further compare our approach against previous state-of-the-art methods on cross-dataset scenarios. As shown in Table 2, GUMLP obtains the best results in all scenes and all metrics, consistently surpassing other methods. After utilizing the UAO framework, the performance can be further improved in both indoor and outdoor scenarios. This suggests that the designed testing-time optimization process can effectively enhance the model’s ability to generalize to unknown actions and datasets.

5.4. Ablation Study

Impact of Constraints during Optimization. In the absence of ground truth labels, it is crucial to set appropriate targets for testing-time optimization to achieve high-quality 3D poses. To this end, we evaluate the effectiveness of two proposed constraints in the optimization process. Table 3 presents the ablation results of 5 iterations using the UAO framework on the test set of Human3.6M. The results reveal that the projection constraint leads to a significant performance improvement of the pure data-driven method (from 49.5mm to 48.2mm). Furthermore, the introduction of the uncertainty constraint brings further improvements in MPJPE, with the metric reaching 47.2mm. These experimental re-

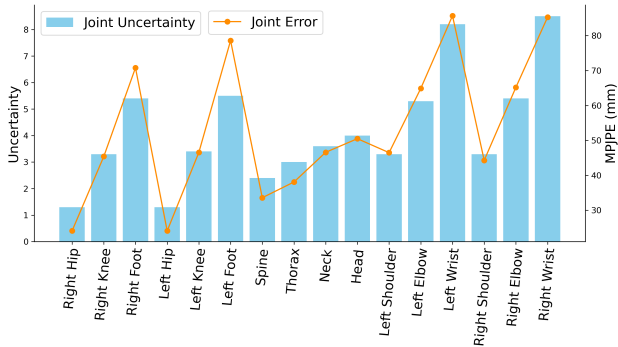


Figure 5. Combination of a histogram representing the uncertainty for each joint and a line chart depicting the mean error (MPJPE) for each joint. The left y-axis denotes the magnitude of uncertainty, while the right y-axis signifies the error value.

Table 4. Inference speed of various optimization methods. UAO* signifies employing the network’s latent state as the variable for optimization.

Method	FPS	MPJPE ↓
Model-only	310	49.5
BOA [8]	19	48.5
ISO [41]	18	<u>47.9</u>
UAO	48	47.2
UAO*	<u>125</u>	47.7

sults demonstrate the effectiveness of these two constraints. To further explore the optimization mechanism, we illustrate the performance with different iterations on the test set of Human3.6M, as shown in Figure 4. We observe that using only the projection constraint leads to a rapid decrease in MPJPE, followed by a gradual increase. In contrast, the error can be stabilized at a lower level with the further introduction of uncertainty constraint, even with more iterations. The main reason is that the projection constraint only ensures the consistency of the projected pose in the 2D plane, which is easy to overfitting, yielding unrealistic poses in the 3D space. For complementary, the uncertainty constraint ensures the output remains close to the 3D manifold, which restricts joints with low uncertainty from deviating too far from the ground truth while allowing joints with high uncertainty to have more optimization flexibility. The experimental results showcase the robust adaptability of our method, especially in real-world scenarios where the optimal number of iterations is uncertain.

Impact of Optimization Strategies. We evaluated the inference speed of various optimization strategies on a single frame using one GeForce RTX 3090, results are shown in Table 4. We use GUMLP as the baseline model, achieving **310** fps. By setting the number of iterations as 4, our UGO framework reaches **48** fps, outperforming the speed

Table 5. Performance across different views on Human3.6M in MPJPE. In-domain refers to testing under the same view as the training, while out-of-domain refers to testing under views other than the training view. P_i denotes the i th camera view.

Training views	In Domain			Out-of-Domain		
	GUMLP	+ UAO	Δ	GUMLP	+ UAO	Δ
P_1	54.3	51.9	2.4	92.2	89.4	2.8
P_1, P_2	50.9	48.1	2.8	67.8	63.7	4.1
P_1, P_2, P_3	50.5	48.0	2.5	60.3	54.7	5.6
P_1, P_2, P_3, P_4	49.5	47.2	2.3	-	-	-

of both the teacher-student approach used in BOA [8] and the Inference Stage Optimization (ISO) [41] approach. This is because our UAO framework optimize the latent state \mathbf{z} rather than the entire model parameters, resulting in accelerated inference. Despite this reduction, the performance still meets real-time requirements. It is worth noting that the output of any layer within the network can be selected as the latent state for optimization. Here, we select the latent state before the final fully connected layer as the optimized variable, termed UAO*. This choice brings a significant surge in inference speed, reaching up to **125** fps. Such an alteration allows faster processing while maintaining satisfactory performance.

5.5. Uncertainty and Error for each Joint

Figure 5 shows the average uncertainty and average error for each joint estimation across the entire test set, using the GUMLP model pre-trained on the human3.6M dataset. For uncertainty estimation, we observe that the joints at the end of limbs often exhibit significant predicted uncertainty, such as the left wrist and the left foot. This phenomenon is attributed to the fact that joints at the ends of the limbs typically experience higher movement velocities, presenting challenges in accurate prediction. Moreover, the line chart illustrating joint errors follows a trend similar to the histogram, indicating that joints with larger uncertainties generally exhibit higher prediction errors. This further validates the effectiveness of GUMLP in predicting joint uncertainties.

5.6. Generalization to Unseen Camera Views

Table 5 presents the relative gains of the proposed approach over in- and out-domain cases on Human3.6M, where four camera views are available. It can be inferred that the UAO framework can not only help the in-domain cases but also bring more significant improvements to unseen camera views. This verifies its ability to break the domain gap and meet our design expectations. Besides, from the last column of the table, a large training set can bring more optimization gains, which may be explained by better pre-training leading to a better depiction of the 3D pose manifold.

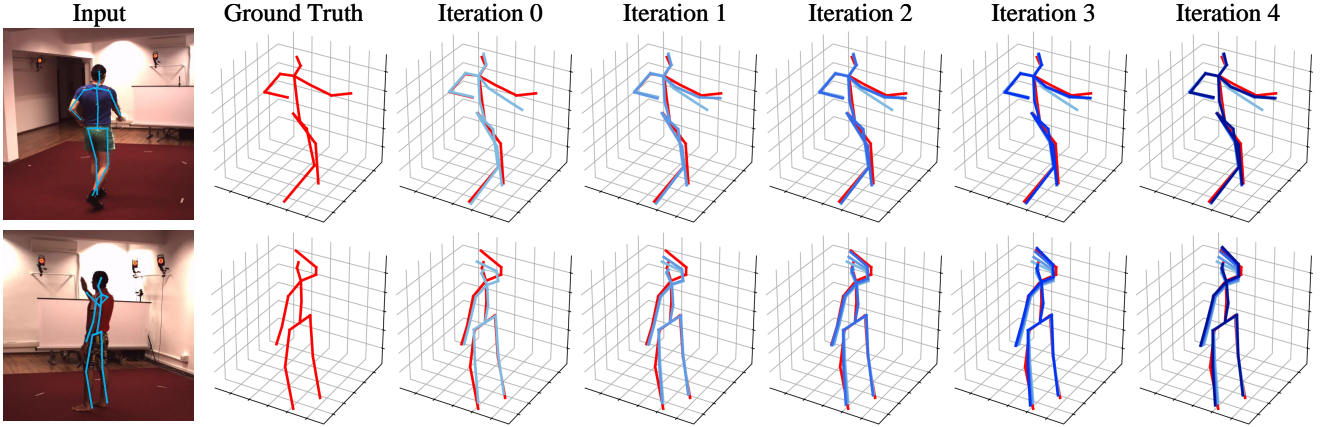


Figure 6. Visualization of the iterative optimization process. The red pose is the ground truth and the blue pose is our prediction. Color intensity reflects the number of iterations, with darker colors indicating more iterations. The initial 3D pose generated by the pre-trained model (column 3) progressively improves through iterative optimization (columns 4-7).

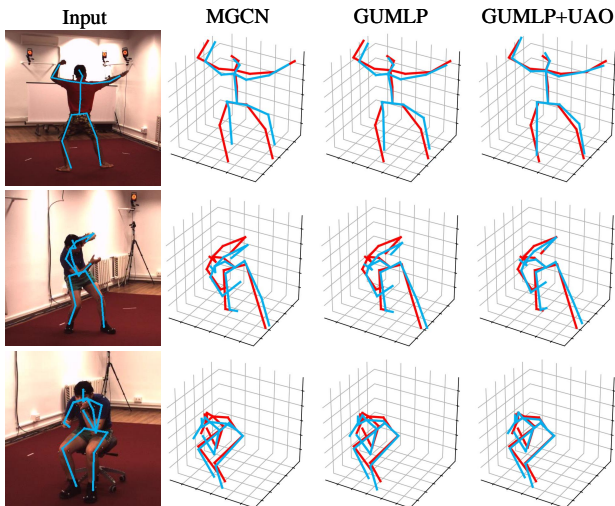


Figure 7. Quantitative comparison of MGCN [47], GUMLP, and GUMLP with UAO on Human3.6M. The blue pose represents the predicted results, while the red pose represents the ground truth.

5.7. Qualitative Results

The visualization results on the Human3.6M dataset are shown in Figure 7. We can see that our original GUMLP is marginally superior to the previous state-of-the-art method, MGCN [47]. Moreover, employing the UAO framework brings better generation with more precise poses. For example, the 3D pose of photoing action (row 2) predicted by GUMLP with UAO (col 4) is similar to the ground truth. As a comparison, the left arms predicted by MGCN and the GUMLP are at a lower position. We further visualize the iterative process of the UAO framework, as shown in Figure 6. After four iterations of optimization, the original

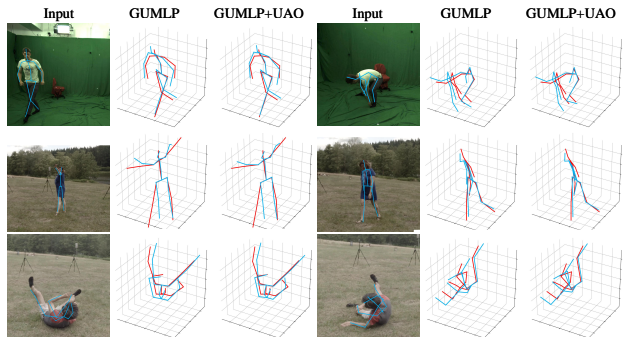


Figure 8. Qualitative results of our method on indoor and outdoor scenes on the MPI-INF-3DHP dataset.

3D output of GUMLP (col 3) becomes more reasonable and accurate in detail, highlighting the effectiveness of the optimization process. Figure 8 shows the qualitative results on MPI-INF-3DHP test set. It can be seen that our approach exhibits commendable performance in both indoor and outdoor scenarios.

6. Conclusion

In this paper, we propose an Uncertainty-Aware testing-time Optimization (UAO) framework for 3D human pose estimation. During the training process, we propose the GUMLP to estimate 3D results and uncertainty values for each joint. For test-time optimization, our UAO framework freezes the pre-trained network parameters and optimizes a latent state initialized by the input 2D pose. To constrain the optimization direction in both 2D and 3D spaces, projection and uncertainty constraints are applied. Extensive experiments show that our approach achieves state-of-the-art performance on two popular datasets.

References

- [1] Jimmy Lei Ba, Jamie Ryan Kiros, and Geoffrey E Hinton. Layer normalization. *arXiv preprint arXiv:1607.06450*, 2016.
- [2] Yujun Cai, Liuhaog Ge, Jun Liu, Jianfei Cai, Tat-Jen Cham, Junsong Yuan, and Nadia Magnenat Thalmann. Exploiting spatial-temporal relationships for 3D pose estimation via graph convolutional networks. In *ICCV*, pages 2272–2281, 2019.
- [3] Yilun Chen, Zhicheng Wang, Yuxiang Peng, Zhiqiang Zhang, Gang Yu, and Jian Sun. Cascaded pyramid network for multi-person pose estimation. In *CVPR*, pages 7103–7112, 2018.
- [4] Hai Ci, Chunyu Wang, Xiaoxuan Ma, and Yizhou Wang. Optimizing network structure for 3D human pose estimation. In *ICCV*, pages 2262–2271, 2019.
- [5] Mohsen Gholami, Bastian Wandt, Helge Rhodin, Rabab Ward, and Z Jane Wang. Adaptpose: Cross-dataset adaptation for 3D human pose estimation by learnable motion generation. In *CVPR*, pages 13075–13085, 2022.
- [6] Xavier Glorot, Antoine Bordes, and Yoshua Bengio. Deep sparse rectifier neural networks. In *Proceedings of the fourteenth international conference on artificial intelligence and statistics*, pages 315–323. JMLR Workshop and Conference Proceedings, 2011.
- [7] Kehong Gong, Jianfeng Zhang, and Jiashi Feng. PoseAug: A differentiable pose augmentation framework for 3D human pose estimation. In *CVPR*, pages 8575–8584, 2021.
- [8] Shanyan Guan, Jingwei Xu, Michelle Z He, Yunbo Wang, Bingbing Ni, and Xiaokang Yang. Out-of-domain human mesh reconstruction via dynamic bilevel online adaptation. *IEEE Transactions on Pattern Analysis and Machine Intelligence*, 2022.
- [9] Md Tanvir Hassan and A Ben Hamza. Regular splitting graph network for 3d human pose estimation. *IEEE Transactions on Image Processing*, 2023.
- [10] Dan Hendrycks and Kevin Gimpel. Gaussian error linear units (GELUs). *arXiv preprint arXiv:1606.08415*, 2016.
- [11] Mengxian Hu, Chengju Liu, Shu Li, Qingqing Yan, Qin Fang, and Qijun Chen. A geometric knowledge oriented single-frame 2D-to-3D human absolute pose estimation method. *IEEE Transactions on Circuits and Systems for Video Technology*, 2023.
- [12] Hanbyul Joo, Natalia Neverova, and Andrea Vedaldi. Exemplar fine-tuning for 3D human model fitting towards in-the-wild 3D human pose estimation. In *3DV*, pages 42–52. IEEE, 2021.
- [13] Laurent Valentin Jospin, Hamid Laga, Farid Boussaid, Wray Buntine, and Mohammed Bannamoun. Hands-on bayesian neural networks—a tutorial for deep learning users. *IEEE Computational Intelligence Magazine*, 17(2):29–48, 2022.
- [14] Mira Kim, Youngjo Min, Jiwon Kim, and Seungryong Kim. Meta-learned initialization for 3D human recovery. In *ICIP*, pages 4238–4242, 2022.
- [15] Nikos Kolotouros, Georgios Pavlakos, Michael J Black, and Kostas Daniilidis. Learning to reconstruct 3D human pose and shape via model-fitting in the loop. In *ICCV*, pages 2252–2261, 2019.
- [16] Han Li, Bowen Shi, Wenrui Dai, Hongwei Zheng, Botao Wang, Yu Sun, Min Guo, Chenglin Li, Junni Zou, and Hongkai Xiong. Pose-oriented transformer with uncertainty-guided refinement for 2D-to-3D human pose estimation. In *AAAI*, pages 1296–1304, 2023.
- [17] Wenhao Li, Hong Liu, Runwei Ding, Mengyuan Liu, Pichao Wang, and Wenming Yang. Exploiting temporal contexts with strided transformer for 3D human pose estimation. *IEEE Transactions on Multimedia*, 2022.
- [18] Wenhao Li, Hong Liu, Hao Tang, Pichao Wang, and Luc Van Gool. MHFormer: Multi-hypothesis transformer for 3D human pose estimation. In *CVPR*, pages 13147–13156, 2022.
- [19] Mengyuan Liu, Hong Liu, and Chen Chen. Enhanced skeleton visualization for view invariant human action recognition. *Pattern Recognition*, 68:346–362, 2017.
- [20] Xiaoxuan Ma, Jiajun Su, Chunyu Wang, Hai Ci, and Yizhou Wang. Context modeling in 3D human pose estimation: A unified perspective. In *CVPR*, pages 6238–6247, 2021.
- [21] Julieta Martinez, Rayat Hossain, Javier Romero, and James J Little. A simple yet effective baseline for 3D human pose estimation. In *ICCV*, pages 2640–2649, 2017.
- [22] Georgios Pavlakos, Xiaowei Zhou, Konstantinos G Derpanis, and Kostas Daniilidis. Coarse-to-fine volumetric prediction for single-image 3D human pose. In *CVPR*, pages 7025–7034, 2017.
- [23] Dario Pavllo, Christoph Feichtenhofer, David Grangier, and Michael Auli. 3D human pose estimation in video with temporal convolutions and semi-supervised training. In *CVPR*, pages 7753–7762, 2019.
- [24] Varun Ramakrishna, Takeo Kanade, and Yaser Sheikh. Reconstructing 3D human pose from 2D image landmarks. In *ECCV*, pages 573–586, 2012.
- [25] Olaf Ronneberger, Philipp Fischer, and Thomas Brox. U-Net: Convolutional networks for biomedical image segmentation. In *MICCAI*, pages 234–241, 2015.
- [26] Edgar Simo-Serra, Arnau Ramisa, Guillem Alenya, Carme Torras, and Francesc Moreno-Noguer. Single image 3D human pose estimation from noisy observations. In *CVPR*, pages 2673–2680, 2012.
- [27] Ke Sun, Bin Xiao, Dong Liu, and Jingdong Wang. Deep high-resolution representation learning for human pose estimation. In *CVPR*, pages 5693–5703, 2019.
- [28] Xiao Sun, Bin Xiao, Fangyin Wei, Shuang Liang, and Yichen Wei. Integral human pose regression. In *ECCV*, pages 529–545, 2018.
- [29] Mikael Svenstrup, Soren Tranberg, Hans Jorgen Andersen, and Thomas Bak. Pose estimation and adaptive robot behaviour for human-robot interaction. In *ICRA*, pages 3571–3576, 2009.
- [30] Zhenhua Tang, Jia Li, Yanbin Hao, and Richang Hong. Mlp-jcg: Multi-layer perceptron with joint-coordinate gating for efficient 3d human pose estimation. *IEEE Transactions on Multimedia*, 2023.
- [31] Antti Tarvainen and Harri Valpola. Mean teachers are better role models: Weight-averaged consistency targets improve semi-supervised deep learning results. In *NeurIPS*, page 1195–1204, 2017.

- [32] Ashish Vaswani, Noam Shazeer, Niki Parmar, Jakob Uszkoreit, Llion Jones, Aidan N Gomez, Łukasz Kaiser, and Illia Polosukhin. Attention is all you need. In *NeurIPS*, pages 5998–6008, 2017.
- [33] Chunyu Wang, Yizhou Wang, Zhouchen Lin, Alan L Yuille, and Wen Gao. Robust estimation of 3D human poses from a single image. In *CVPR*, pages 2361–2368, 2014.
- [34] Scott Workman, Connor Greenwell, Menghua Zhai, Ryan Baltenberger, and Nathan Jacobs. Deepfocal: A method for direct focal length estimation. In *ICIP*, pages 1369–1373. IEEE, 2015.
- [35] Tianhan Xu and Wataru Takano. Graph stacked hourglass networks for 3D human pose estimation. In *CVPR*, pages 16105–16114, 2021.
- [36] Jae Shin Yoon, Lingjie Liu, Vladislav Golyanik, Kripasindhu Sarkar, Hyun Soo Park, and Christian Theobalt. Pose-guided human animation from a single image in the wild. In *CVPR*, pages 15039–15048, 2021.
- [37] Ailing Zeng, Xiao Sun, Fuyang Huang, Minhao Liu, Qiang Xu, and Stephen Lin. SRNet: Improving generalization in 3D human pose estimation with a split-and-recombine approach. In *ECCV*, pages 507–523, 2020.
- [38] Ailing Zeng, Xiao Sun, Lei Yang, Nanxuan Zhao, Minhao Liu, and Qiang Xu. Learning skeletal graph neural networks for hard 3D pose estimation. In *ICCV*, pages 11436–11445, 2021.
- [39] Kai Zhai, Qiang Nie, Bo Ouyang, Xiang Li, and ShanLin Yang. Hopfir: Hop-wise graphformer with intragroup joint refinement for 3d human pose estimation. *arXiv preprint arXiv:2302.14581*, 2023.
- [40] Hongwen Zhang, Yating Tian, Xinchu Zhou, Wanli Ouyang, Yebin Liu, Limin Wang, and Zhenan Sun. Pymaf: 3D human pose and shape regression with pyramidal mesh alignment feedback loop. In *ICCV*, pages 11446–11456, 2021.
- [41] Jianfeng Zhang, Xuecheng Nie, and Jiashi Feng. Inference stage optimization for cross-scenario 3D human pose estimation. In *NeurIPS*, pages 2408–2419, 2020.
- [42] Jinlu Zhang, Zhigang Tu, Jianyu Yang, Yujin Chen, and Jun-song Yuan. MixSTE: Seq2seq mixed spatio-temporal encoder for 3D human pose estimation in video. In *CVPR*, pages 13232–13242, 2022.
- [43] Shengping Zhang, Chenyang Wang, Liqiang Nie, Hongxun Yao, Qingming Huang, and Qi Tian. Learning enriched hop-aware correlation for robust 3d human pose estimation. *IJCV*, 131(6):1566–1583, 2023.
- [44] Long Zhao, Xi Peng, Yu Tian, Mubbasir Kapadia, and Dimitris N Metaxas. Semantic graph convolutional networks for 3D human pose regression. In *CVPR*, pages 3425–3435, 2019.
- [45] Weixi Zhao, Weiqiang Wang, and Yunjie Tian. GraFormer: Graph-oriented transformer for 3D pose estimation. In *CVPR*, pages 20438–20447, 2022.
- [46] Ce Zheng, Sijie Zhu, Matias Mendieta, Taojiannan Yang, Chen Chen, and Zhengming Ding. 3D human pose estimation with spatial and temporal transformers. In *ICCV*, pages 11656–11665, 2021.
- [47] Zhiming Zou and Wei Tang. Modulated graph convolutional network for 3d human pose estimation. In *ICCV*, pages 11477–11487, 2021.

Supplementary Material

This supplemental material contains the following parts:

- Theory of uncertainty estimation (Sec. A).
- Brief introduction of GCN (Sec. B).
- Additional quantitative results (Sec. C).
- Additional ablation studies (Sec. D).
- Effectiveness of the UAO framework (Sec. E).
- Limitations (Sec. F).

A. Theory of Uncertainty Estimation

Assuming the 3D pose follows Gaussian distributions, we reformulate the 2D-to-3D network as a Bayesian Neural Network (BNN) [13], which estimates a Gaussian distribution of the target rather than only predicting the absolute coordinates of points. Specifically, for the 3D joints \mathbf{J}_i of person i in the dataset, our goal is to estimate the distribution of 3D joints for that individual. During training, the objective is to maximize the likelihood of all observation pairs. The likelihood function can be formulated as follows:

$$Likelihood = \prod_{i,k} \mathcal{N}(\mathbf{J}_{i,k} | \boldsymbol{\mu}_{i,k}, \Sigma_{i,k}), \quad (7)$$

where k is the index for the k -th joint of a person, $\boldsymbol{\mu}_{i,k}$ represents the mean, $\Sigma_{i,k}$ represents the covariance matrix of the Gaussian distribution for the k -th joint of person i . Each joint is considered as a random variable following a normal Gaussian distribution. To further elaborate, the mean $\boldsymbol{\mu}_{i,k}$ captures the most probable location of the k -th joint, while the covariance matrix $\Sigma_{i,k}$ characterizes the uncertainty of the distribution around this mean. The likelihood term models the probability of observing the actual 3D joint positions given the estimated means and covariances. In pursuit of the most accurate estimation of the 3D joint positions, we seek the maximum likelihood, which aligns the estimated Gaussian distribution with the observed 3D joint positions, capturing both the most probable locations $\boldsymbol{\mu}_{i,k}$ and the uncertainty $\Sigma_{i,k}$ associated with each joint. The formulation of the maximum likelihood function can be achieved by:

$$\begin{aligned} \theta^* &= \arg \max_{\theta} \sum_{i,k} \log \mathcal{N}(\mathbf{J}_{i,k} | \boldsymbol{\mu}_{i,k}, \Sigma_{i,k}) \\ &= \arg \min_{\theta} \frac{1}{2K} \sum_{i,k} \left((\mathbf{J}_{i,k} - \boldsymbol{\mu}_{i,k})^T \Sigma_{i,k}^{-1} (\mathbf{J}_{i,k} - \boldsymbol{\mu}_{i,k}) \right. \\ &\quad \left. + \ln |\Sigma_{i,k}| \right). \end{aligned} \quad (8)$$

Here we simplify the covariance matrix $\Sigma_{i,k}$ as a diagonal matrix with diagonal elements $\sigma_{i,k}^2$, then we get:

$$\theta^* = \arg \min_{\theta} \frac{1}{2K} \sum_{i,k} \left(\frac{\|\mathbf{J}_{i,k} - \boldsymbol{\mu}_{i,k}\|^2}{\sigma_{i,k}^2} + \ln \sigma_{i,k}^2 \right). \quad (9)$$

We set $\mathbf{s}_{i,k} = \ln \sigma_{i,k}^2$, our target can be reformulated as:

$$\theta^* = \arg \min_{\theta} \frac{1}{2K} \sum_{i,k} \left(\frac{\|\mathbf{J}_{i,k} - \boldsymbol{\mu}_{i,k}\|^2}{\exp(\mathbf{s}_{i,k})} + \mathbf{s}_{i,k} \right). \quad (10)$$

Through this formulation, we can minimize the discrepancy between the predicted mean $\boldsymbol{\mu}_i$ and the ground truth \mathbf{J}_i while accounting for the associated uncertainty \mathbf{s}_i . This approach ensures that the estimated Gaussian distribution aligns optimally with the observed 3D joints, providing a robust and reliable characterization of the underlying 3D pose distribution.

B. Graph Convolutional Network

Graph Convolutional Network (GCN) is capable to capture intricate relationships and structures within graph-structured data. Consider an undirected graph as $G = \{V, E\}$, where V is the set of nodes, and E is the set of edges. The edges can be encoded in an adjacency matrix $A \in \{0, 1\}^{N \times N}$. For the input X_l of the l^{th} layer, the vanilla graph convolution aggregates the features of the neighboring nodes. The output X_{l+1} of the l^{th} GCN layer can be formulated as:

$$X_{l+1} = \sigma \left(\tilde{D}^{-\frac{1}{2}} \tilde{A} \tilde{D}^{-\frac{1}{2}} X_l W \right), \quad (11)$$

where σ is the ReLU activation function [6], $W_l \in \mathbb{R}^{d_1 \times d}$ is the layer-specific trainable weight matrix. $\tilde{A} = A + I_N$ is the adjacency matrix of the graph with added self-connections, where I_N is the identity matrix. Additionally, \tilde{D} is the diagonal node degree matrix. By stacking multiple GCN layers, it iteratively transforms and aggregates neighboring nodes, thereby obtaining enhanced feature representations. For the task of 3D human pose estimation, GCN it can effectively capture of the semantic information of the human skeleton.

C. Quantitative Results under Protocol 2

Table 6 compares the performance of our approach with other state-of-the-art methods on Human3.6M under Protocol 2. Following previous approaches [2, 35, 47], the 2D pose detected by CPN [3] is used as input. The experimental results show that our GUMLP achieves competitive results. Furthermore, the performance of GUMLP under Protocol 2 can be further improved when using the UAO framework, surpassing all previous methods.

D. Additional Ablation Studies

Impact of λ_P and λ_U . During testing-time optimization, we applied constraints to ensure alignment of the generated poses in both 2D and 3D spaces. Table 7 shows the impact of the hyperparameters for the projection loss (λ_P) and uncertainty loss (λ_U). Here we set $\lambda_P = 1$ for projection loss and

Table 6. Quantitative comparison with the state-of-the-art methods on Human3.6M under Protocol 2. The 2D pose detected by cascaded pyramid network (CPN) [3] is used as input. § denotes the methods that use refinement module [2, 47]. The top two best results for each action are highlighted in bold and underlined, respectively.

Protocol 2	Dire.	Disc.	Eat	Greet	Phone	Photo	Pose	Purch.	Sit	SitD.	Smoke	Wait	WalkD.	Walk	WalkT.	Avg
SimpleBaseline (ICCV’2017) [21]	39.5	43.2	46.4	47.0	51.0	56.0	41.4	40.6	56.5	69.4	49.2	45.0	49.5	38.0	43.1	47.7
VideoPose3D (CVPR’2019) [23]	36.0	38.7	38.0	41.7	40.1	45.9	37.1	35.4	46.8	53.4	41.4	36.9	43.1	30.3	34.8	40.0
LCN (ICCV’2019) [4]	36.9	41.6	38.0	41.0	41.9	51.1	38.2	37.6	49.1	62.1	43.1	39.9	43.5	32.2	37.0	42.2
STGCN (ICCV’2019) [2]§	36.8	38.7	38.2	41.7	40.7	46.8	37.9	35.6	47.6	51.7	41.3	36.8	42.7	31.0	34.7	40.2
SRNet (ECCV’2020) [37]	35.8	39.2	36.6	36.9	39.8	45.1	38.4	36.9	47.7	54.4	38.6	36.3	39.4	30.3	35.4	39.4
MGCN (ICCV’2021) [47]§	35.7	38.6	36.3	40.5	39.2	<u>44.5</u>	37.0	35.4	46.4	51.2	40.5	35.6	41.7	30.7	33.9	<u>39.1</u>
MLP-JCG (TMM’2023) [30]	33.7	37.4	37.3	<u>39.6</u>	39.8	47.1	33.7	33.8	45.7	60.5	<u>39.7</u>	37.7	<u>40.1</u>	<u>30.1</u>	<u>33.8</u>	39.3
GKONet (TCSVT’2023) [11]	35.4	38.8	<u>35.9</u>	40.4	<u>39.6</u>	44.0	36.7	35.4	46.8	53.7	40.9	36.6	42.0	30.6	33.9	39.4
GUMLP (Ours)	35.3	38.5	<u>35.9</u>	40.2	40.3	44.9	<u>36.3</u>	35.0	<u>46.2</u>	<u>51.8</u>	41.2	<u>35.8</u>	41.7	30.3	33.9	39.2
GUMLP + UAO (Ours)	<u>34.9</u>	<u>38.3</u>	35.3	40.2	40.1	44.9	36.5	<u>34.8</u>	<u>46.0</u>	51.9	40.8	36.0	42.3	30.0	33.4	39.0

Table 7. Influence of projection loss (λ_P) and uncertainty loss (λ_U) hyperparameters.

λ_P	λ_U	Best Iteration	MPJPE
1.0	0.000	3	47.6
	0.005	5	47.2
	0.010	8	47.5
	0.015	10	47.9
	0.020	9	48.4

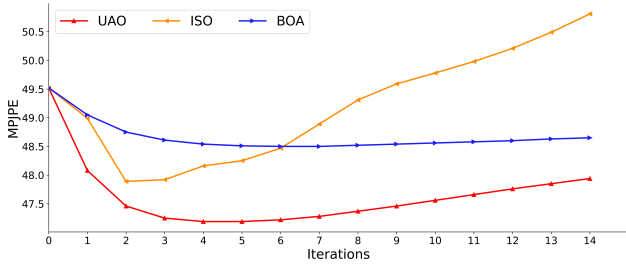


Figure 9. Performance with different iterations on Human3.6M test set. Here we adopt the pre-trained GUMLP as baseline and use the 2D pose detected by CPN [3] to initialize the latent state \mathbf{z} .

explore the impact of the hyperparameter λ_U for uncertainty loss. As the uncertainty loss regulates the degree to which the 3D pose updates can deviate from the initial estimation, a small or large value of λ_U will influence the performance. For better performance, the final hyperparameters selected in our experiments are $\lambda_P = 1.0$ and $\lambda_U = 0.005$.

E. Effectiveness of the UAO Framework

We have introduced the optimization strategy of the proposed UAO framework in Sec 4.1 of the main text. By freezing the pre-trained model parameters and selecting a hidden state \mathbf{z} as the optimized variable, we establish a robust testing-time optimization approach. In this section, we further validate the effectiveness of UAO framework.

Comparison with other optimization-based methods. We further compare our method with vanilla ISO [41] and BOA

Algorithm 2 Online Adaptation of BOA

Input: 2D poses $\{\mathbf{J}_j^{2D}\}_{j=1}^N$ from test set, pre-trained model M_{ϕ_0} that parameterized by ϕ_0 , moving average rate α of the teacher model M_ω that parameterized by ω , learning rate η , projection matrix \mathbf{P} , optimization steps T

Output: 3D pose $\hat{\mathbf{J}}_j^{3D}$

- 1: Initialization: $\omega = \phi_0$
- 2: **for** $j = 1$ to N **do**
- 3: $\phi_j = \phi_{j-1}$
- 4: **for** $i = 0$ to T **do**
- 5: $\hat{\mathbf{J}}_j^{3D} = M_{\phi_j}(\mathbf{J}_j^{2D})$
- 6: $L^{opt} = \|\hat{\mathbf{J}}_j^{3D} \cdot \mathbf{P} - \mathbf{J}_j^{2D}\|_2$
- 7: $\phi_j = \phi_j - \eta \cdot \nabla L^{opt}$
- 8: **end for**
- 9: # update the teacher model
- 10: $\omega = (1 - \alpha) \cdot \omega + \alpha \cdot \phi_j$
- 11: # predict 3D pose by the teacher model
- 12: $\hat{\mathbf{J}}_j^{3D} = M_\omega(\mathbf{J}_j^{2D})$
- 13: **end for**

[8], two typical testing-time optimization methods. Both of them seek for better generalization capabilities through fine-tuning the network on the test set. The ISO adopts an early-stop mechanism, which requires reloading the pre-trained parameters each time new data is encountered. On the other hand, the BOA adopts a teacher model [31], requiring the loading of model parameters only once and continuously updating them through test data. The implementation details of BOA are summarized in Algorithm 2. Using the pre-trained GUMLP model as baseline, the comparison of the average performance across different iterations is illustrated in Figure 9. The results show that our UAO framework achieves the best performance, demonstrating its superiority. Additionally, the UAO framework optimizes only a hidden state \mathbf{z} rather than the entire network parameters, thereby requiring the storage of a small number of parameters. As presented in Table 5 in the main text, UAO attains the highest inference speed, making it more suitable for online inference

Table 8. Performance of other data-driven models with UAO framework in MPJPE. MF represents multi-frame methods, and SF represents single-frame methods. GT denotes the method adopts ground truth 2D input.

Method		Original	+ UAO	Δ
MF	MHFormer [18]	43.0	40.8	2.2
	MixSTE [42]	40.9	39.9	1.0
	PoseFormer [46]	44.3	43.2	1.1
SF	SimpleBaseline [21]	53.0	50.2	2.8
	SemGCN [44] (GT)	42.6	42.0	0.6
	MGCN [47]	49.4	47.9	1.5

scenarios.

Extension to Other Data-Driven Models. To evaluate the general applicability of the UAO framework, we test its performance on other data-driven models. For simplicity, here we only adopt the projection constraint during testing-time optimization. The results are presented in Table 8. The outcomes clearly indicate a substantial performance enhancement for both multi-frame and single-frame models through the implementation of testing-time optimization paradigms. The experimental results underscore the generalization of our UAO framework, showcasing its adaptability and ease of extension to other pre-trained models.

F. Limitations

The uncertainty constraint serves as a balancing factor between the optimization direction and the initial results. When dealing with joints that already have accurate initial estimates, two scenarios arise: (a) relying solely on the projection constraint might deteriorate the results. In this setting, our uncertainty constraint can effectively alleviate this problem; (b) relying solely on the projection constraint can also bring the optimized results closer to the ground truth. In this case, the uncertainty constraint will limit the optimization process.